nature communications

Article

https://doi.org/10.1038/s41467-026-74446-6

Epigenetic compartmentalization of mitotic chromosomes by phase-separation-driven repulsion between WDR5 and the chromosomal passenger complex

Received: 26 November 2025

Accepted: 8 June 2026

Published online: 16 June 2026

Check for updates

Yun Wang[1,5], Xianyun Jiang[2,5], Xing Liu[1,5], Xin Jiang[1], Xiyu Wang[1], Xiaoyu Song[1], Feng Chen[1], Yuanyuan Liu[1], Xu-Zhuo Gou[1,3], Ai-Hui Tang[1,3], Sibei Sheng[4] ✉, Xuebiao Yao[1] ✉, Zhonghuai Hou[2] ✉ & Dan Liu[1] ✉

Histone modifications recruit chromatin regulators, but how their spatial patterns are established on mitotic chromosomes remains unclear. Spatial separation between active chromatin and centromeric signaling is essential for accurate chromosome segregation, yet the physical principles linking epigenetic marks to mitotic protein organization are poorly defined. Here, we show that liquid-liquid phase separation (LLPS) of WDR5, a core component of H3K4 methyltransferase complexes, acts as a spatial organizer of mitotic chromosomes. WDR5 LLPS is driven by multivalent charged and hydrophobic interactions in its N-terminal region. Phase-separated WDR5 repels the chromosomal passenger complex (CPC), segregating H3K4-trimethylated (H3K4me3) chromatin from H3T3-phosphorylated (H3T3ph) centromeric regions. Disrupting WDR5 condensation causes Aurora B mislocalization and chromosome misalignment, and restoring H3K4me3 alone does not rescue these defects. Computational modeling and rescue experiments support that WDR5-driven LLPS and histone modification signals cooperate to concentrate CPC at centromeres, revealing how LLPS and epigenetic information organize chromatin compartments during mitosis.

The precise spatial organization of chromatin is fundamental to genome function[1,2], orchestrating genomic integrity[3], and cellular identity[4]. Compartmentalization of chromatin-associated proteins enables the segregation of biochemical activities[5–7], ensuring that complex nuclear processes are conducted with high specificity and fidelity. This spatial coordination becomes particularly crucial during mitosis, when chromosomes undergo dramatic structural reorganization while retaining functionally distinct domains to ensure accurate segregation[8], a process whose failure underlies aneuploidy and oncogenesis[9]. Histone modifications constitute a central mechanism of chromatin regulation[10,11]. These epigenetic marks serve as biochemical platforms that recruit specific chromatin regulators to defined genomic domains, thereby directing processes such as gene expression[12], DNA repair[13], and chromosome segregation[14]. However,

[1]MOE Key Laboratory for Membraneless Organelles and Cellular Dynamics, Hefei National Research Center for Physical Sciences at the Microscale, Division of Life Sciences and Medicine, University of Science and Technology of China, Hefei, China. [2]Department of Chemical Physics, Hefei National Research Center for Physical Sciences at the Microscale, University of Science and Technology of China, Hefei, China. [3]Laboratory of Biomedical Imaging and Intelligent Processing, Institute of Artificial Intelligence, Hefei Comprehensive National Science Center, Hefei, China. [4]Yingshanhong Intelligent (Shanghai) Testing Technology Co., Ltd., Shanghai, China. [5]These authors contributed equally: Yun Wang, Xianyun Jiang, Xing Liu. ✉e-mail: shengsibei@ustc.edu.cn; yaoxb@ustc.edu.cn; hzhlj@ustc.edu.cn; dliu919@ustc.edu.cn

the mechanisms by which histone modifications achieve precise spatial patterns remain incompletely understood, especially considering that many chromatin-modifying enzymes and their nucleosome substrates are broadly distributed across the genome.

The CPC, comprising Aurora B kinase, INCENP, Survivin, and Borealin, exemplifies this question, which dynamically localizes to centromeres during prometaphase, transits to the spindle midzone in anaphase, and accumulates at the midbody in telophase[15,16]. Centromeric enrichment of the CPC positions Aurora B in proximity to kinetochore substrates, enabling tension-sensitive phosphorylation that corrects improper kinetochore-microtubule attachments and ensures chromosome bi-orientation[17,18]. This specific centromeric targeting requires the recognition of histone H3 threonine 3 phosphorylation (H3T3ph) by Survivin[19–21]—a modification catalyzed by Haspin, a kinase broadly distributed across the chromosome[22]. Elucidating how the CPC achieves such centromeric precision will be helpful for understanding the mechanisms governing chromatin organization.

LLPS has emerged as a principle for organizing biomolecules into functional compartments[23–27]. Indeed, the CPC undergoes LLPS via the intrinsically disordered region (IDR) within Borealin, which is required for its centromeric localization[28,29], and this process is modulated by the MLL1/WDR5 complex through methylation of the IDR[30]. However, the intrinsic LLPS propensity observed in vitro inadequately predicts the centromere-specific localization of the CPC in vivo, and centromeres themselves do not appear to provide an intrinsic platform that directly drives CPC condensation[31]. These observations indicate that neither histone modifications nor LLPS alone fully account for the spatial restriction of the CPC to centromeres, pointing to an unresolved interplay between biochemical and biophysical regulatory layers. In this context, WDR5 arises as an intriguing regulatory node. Beyond its canonical role in directing MLL1-mediated trimethylation of histone H3 at lysine 4 (H3K4me3) for transcriptional regulation[32,33]—a modification that has also been shown to inhibit phosphorylation of histone H3 at threonine 3 (H3T3ph) in vitro[34,35]. WDR5 also interacts with the anaphase-promoting complex (APC/C) to facilitate transcriptional reactivation upon mitotic exit[36]. In contrast, the centromeric domain where the CPC concentrates is composed of constitutive heterochromatin and remains transcriptionally silent. These observations give rise to the possibility that a distinct spatial regulatory mechanism involving WDR5 and the CPC operates during mitosis to ensure the precise execution of their respective functions.

Here, we uncover a non-canonical mitotic function for WDR5 in organizing biophysical chromosome compartments. We demonstrate that the WDR5 IDR drives LLPS, mediating repulsive immiscibility with CPC condensates. This LLPS-driven repulsion spatially segregates H3K4me3-enriched chromosome arms from centromeric H3T3ph domains, effectively restricting CPC to centromeres. Our findings support a spatial regulatory mechanism in which phase separation-driven repulsion between histone writer and reader-associated proteins shapes chromosomal architecture and contributes to membraneless genome compartmentalization.

Results

WDR5 N-terminal IDR drives LLPS and chromosomal localization

We first examined WDR5 localization during mitosis. Immunofluorescence (IF) and live-cell imaging showed that WDR5 associates with mitotic chromosomes (Supplementary Fig. 1a, b). Under 0.4% Triton X-100 permeabilization conditions, WDR5 was preferentially enriched along chromosome arms rather than at centromeres (Fig. 1a). Quantification confirmed significantly higher WDR5 fluorescence intensity on chromosome arms than at centromeres (Fig. 1b). These results indicate that WDR5 exhibits a chromosome arm-biased distribution during mitosis.

During imaging, we also observed droplet-like WDR5 structures around chromosomes, suggesting that it may undergo LLPS (Supplementary Fig. 1a, b). In vitro phase diagram analyses showed that WDR5 spontaneously formed condensates over a range of protein and salt concentrations (Supplementary Fig. 1c, d). In the presence of a macromolecular crowding agent, droplets appeared at concentrations as low as 1.25 μM, supporting physiological relevance (Fig. 1c). Condensate formation was strongly suppressed by high salt or 1,6-hexanediol, indicating that both electrostatic and hydrophobic interactions are key facilitators of WDR5 LLPS (Supplementary Fig. 1d, e). Time-lapse imaging captured droplet fusion (Supplementary Fig. 1f), and FRAP analyses of both in vitro WDR5 condensates (Supplementary Fig. 1g, h) and chromosome-bound puncta in cells (Supplementary Fig. 1i, j) revealed rapid fluorescence recovery, confirming their liquid-like dynamics. Notably, the addition of nucleosome-containing nuclear extract significantly accelerated fluorescence recovery in vitro (Supplementary Fig. 1g, h), suggesting that chromatin-associated components can modulate the mobility and material properties of WDR5 condensates.

To explore the structural basis of this behavior, we used the disorder region predictor D2P2[37] and identified a 32-amino-acid IDR at the N-terminus of WDR5 (Supplementary Fig. 2a). Deletion of this region (WDR5-ΔIDR) severely impaired droplet formation, highlighting its essential role in driving WDR5 LLPS (Fig. 1d). GFP alone did not undergo LLPS, excluding interference from the GFP tag (Fig. 1d). Notably, deletion of the IDR also markedly reduced WDR5 chromosomal localization (Supplementary Fig. 2b, c).

To further test whether WDR5 can undergo condensation in living cells, we employed a light-activated optoDroplet strategy[38]. Upon blue-light stimulation, WDR5 rapidly formed nuclear condensates in COS-7 cells, whereas Cry2 alone did not (Supplementary Fig. 2d). These condensates also underwent fusion events, further supporting their liquid-like behavior (Supplementary Fig. 2e). In contrast, WDR5-ΔIDR failed to form optoDroplets, confirming the essential role of the N-terminal IDR in WDR5 condensation. Moreover, replacing the endogenous WDR5 IDR with the heterologous Pub1 IDR[26] restored condensate formation in the chimeric Pub1_IDR-WDR5-ΔIDR construct, indicating that an exogenous phase-separation domain is sufficient to restore condensate formation (Supplementary Fig. 2d). Together, these findings demonstrate that the N-terminal 32 amino acids of WDR5 are indispensable for its phase separation capacity and are required for its efficient localization to mitotic chromosomes.

WDR5 loss alters mitotic histone marks

To investigate the functional significance of WDR5 during mitosis, we depleted endogenous WDR5 using small interfering RNA (siRNA) and synchronized cells in mitosis for IF analysis. WDR5 knockdown caused pronounced chromosome misalignment (Supplementary Fig. 3a, b), consistent with impaired Aurora B function in correcting erroneous kinetochore-microtubule attachments[17,18]. Indeed, centromeric Aurora B intensity was markedly reduced upon WDR5 depletion (Fig. 1e, f), whereas anti-centromere antibody (ACA) intensity remained unchanged and thus served as a normalization control (Supplementary Fig. 3c). Notably, Aurora B was no longer restricted to centromeres but instead redistributed along chromosome arms (Fig. 1e, g). Consistent with this mislocalization, phosphorylation of CENP-A at serine 7, a direct Aurora B substrate[39], was also reduced at centromeres following WDR5 depletion (Supplementary Fig. 3d, e), confirming compromised Aurora B localization and activity.

Since H3T3ph is known to recruit Aurora B[19–21], we next examined its distribution following WDR5 knockdown. IF analysis showed that H3T3ph was increased along chromosome arms, while decreased at centromeres (Fig. 1h, i), indicating both elevated abundance and altered spatial distribution in the absence of WDR5. For quantification,

https://doi.org/10.1038/s41467-026-74446-6

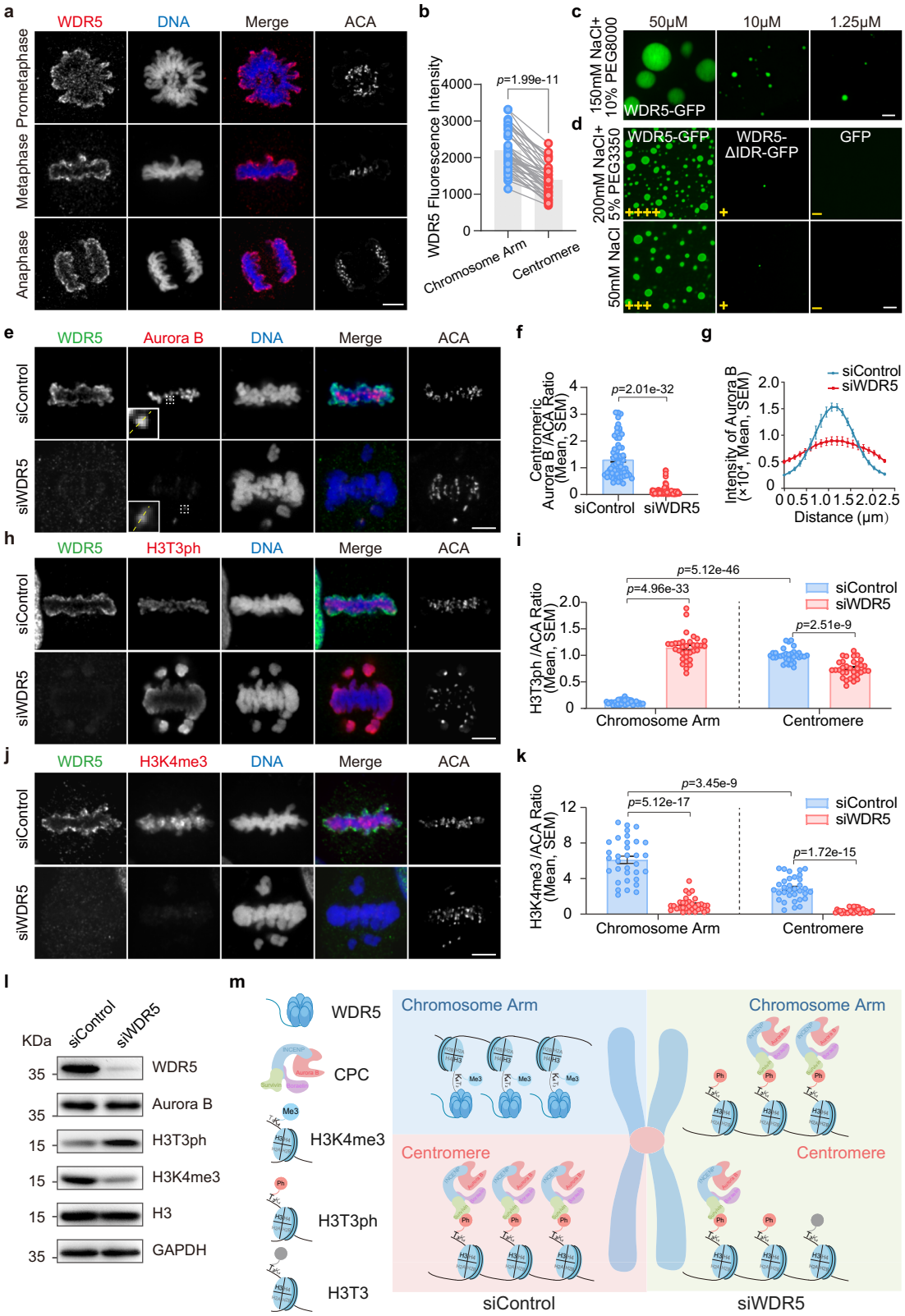

centromeric regions were defined by ACA signals, total chromosomal regions were defined by DNA staining, and chromosome-arm regions were obtained by subtracting ACA-positive regions from the total DNA-defined chromosomal area (Supplementary Fig. 3f). In parallel, H3K4me3, which is mediated by the MLL1–WDR5 complex, was markedly reduced after WDR5 depletion (Fig. 1j, k). In control cells, H3T3ph was predominantly enriched at centromeres, whereas H3K4me3 was mainly localized along chromosome arms (Fig. 1i, k), supporting the existence of spatially distinct chromosomal domains.

In addition, depletion of Aurora B significantly reduced the fluorescence intensity ratio of WDR5 between chromosome arms and centromeres (Supplementary Fig. 3g, h), suggesting that proper CPC/Aurora B function also contributes to maintaining the polarized distribution of WDR5 on mitotic chromosomes. Consistent with these IF

Fig. 1 | Chromosomally localized WDR5 condensates establish distinct H3T3ph and H3K4me3 compartments on chromosomes to maintain Aurora B fidelity. **a** Immunofluorescence images of endogenous WDR5 in HeLa cells stained for WDR5 (red) and DNA (blue). ACA, anti-centromere antibody. **b** Quantification of WDR5 fluorescence intensity on chromosome arms and at centromeres within the same cell. Dots are cells; gray lines connect paired measurements. $n = 43$ cells from four independent experiments; two-tailed paired Student's t test. **c** Representative WDR5 droplets formed with polyethylene glycol 8000 (PEG8000), from three independent experiments with similar results. **d** Confocal images of WDR5-GFP and WDR5-ΔIDR-GFP condensate formation in vitro under the indicated conditions. Protein concentration, 30 μM. '−' indicates no detectable phase separation; '+' indicates detectable phase separation. **e** HeLa cells were treated with control or WDR5 siRNA, synchronized with monastrol, released by washout, treated with MG132, and stained for WDR5 (green), Aurora B (red), and DNA (blue). **f** Quantification of centromeric Aurora B fluorescence intensity normalized to ACA. $n = 65$ and 93 cells from three independent experiments; two-tailed unpaired Student's t test. **g** Line-scan fluorescence intensity profiles across the boxed region in (**e**) magnified 3.5-fold. $n = 10$ cells per group. **h** HeLa cells were processed as in (**e**) and stained for WDR5 (green), H3T3ph (red), and DNA (blue). **i** Quantification of H3T3ph fluorescence intensity on chromosome arms and at centromeres, relative to ACA. $n = 33$ cells per group from three independent experiments; two-tailed unpaired Student's t test. **j** HeLa cells were processed as in (**e**) and stained for WDR5 (green), H3K4me3 (red), and DNA (blue). **k** Quantification of H3K4me3 fluorescence intensity on chromosome arms and at centromeres, relative to ACA. $n = 33$ and 32 cells from three independent experiments; two-tailed unpaired Student's t test. **l** Western blot analysis of WDR5, Aurora B, H3T3ph, and H3K4me3 after control or WDR5 siRNA treatment, representative of three independent experiments with similar results. Molecular weight markers are indicated. **m** Diagram illustrating the redistribution of H3T3 phosphorylation before and after WDR5 knockdown and its competition with Aurora B binding. Scale bars, 5 μm.

results, western blotting (WB) showed that total Aurora B protein levels were not decreased, whereas global H3T3ph levels increased and H3K4me3 levels decreased upon WDR5 depletion (Fig. 1l). Moreover, analysis across the cell cycle showed that total WDR5 protein levels remained relatively constant, and siWDR5 did not alter the overall abundance of Aurora B (Supplementary Fig. 3i). Together, these results indicate that the observed defects arise from redistribution of Aurora B and associated histone modifications, rather than from reduced Aurora B expression. We therefore propose that WDR5 depletion induces ectopic H3T3 hyperphosphorylation on chromosome arms, which may compete with centromeric H3T3ph for Aurora B recruitment (Fig. 1m). Collectively, these data support a model in which H3T3ph and H3K4me3 are spatially compartmentalized on mitotic chromosomes to facilitate efficient Aurora B enrichment at centromeres. To further examine how this spatial segregation is established, we next investigated the distribution patterns of these factors and their molecular interplay.

WDR5-CPC droplets exhibit immiscibility

IF co-staining of H3T3ph and H3K4me3 revealed distinct, largely nonoverlapping distributions across chromosomes (Supplementary Fig. 4a, b). Quantitative colocalization analysis yielded low-to-negative Pearson's coefficients, further supporting their segregation (Supplementary Fig. 4c). However, antibodies recognizing adjacent residues (H3T3 and H3K4) may introduce epitope crowding, potentially obscuring H3K4me3 signals on chromosome arms. We therefore focused on WDR5 and Aurora B, which mark the H3K4me3-enriched and H3T3ph-enriched chromosomal domains, respectively. Representative images, line-scan analyses, and Pearson's correlation measurements consistently showed that WDR5 and Aurora B occupy spatially segregated, largely nonoverlapping compartments on mitotic chromosomes (Fig. 2a–c). Co-staining of H3K4me3 with Aurora B likewise revealed a compartmentalized distribution without potential steric interference between antibodies (Supplementary Fig. 4d–f). Limited overlap at the domain boundary is most likely explained by the close spatial apposition of pericentromeric and centromeric signals at diffraction-limited resolution, rather than complete mixing.

We next examined the temporal emergence of this pattern. In early prophase HeLa cells, WDR5 was not yet prominently chromatin-associated, whereas WDR5 depletion already reduced Aurora B signal on chromosomes (Supplementary Fig. 4g–i). Consistently, quantification of endogenous WDR5 fluorescence from interphase to metaphase showed that chromosomal WDR5 intensity increased from early prophase to prophase and remained elevated through metaphase (Supplementary Fig. 4j, k). Together, these results support the existence of spatially segregated H3T3ph- and H3K4me3-associated chromosomal regions and suggest that both WDR5 and the CPC contribute to the establishment of this organization.

LLPS has been widely recognized as a mechanism for compartmentalizing diverse biochemical processes within cells[23–27]. Notably, the CPC core subcomplex INCENP-Survivin-Borealin (ISB) undergoes LLPS, which contributes to CPC localization and centromere function[28,29]. Building on our evidence that WDR5 also forms condensates and regulates its chromosomal localization, we hypothesized that interactions between the membraneless regions formed by WDR5 and CPC condensates may be crucial for the compartmentalized distribution of H3K4me3 and H3T3ph.

To test this, we purified recombinant WDR5-GFP, mCherry-ISB, and GFP-HP1α and examined their phase behavior in vitro. HP1α was included as a reference because it is a known condensate-forming protein that fully mixes with ISB[28], providing a benchmark for comparison with WDR5. Under identical conditions, all three proteins underwent LLPS (Fig. 2d). Upon mixing mCherry-ISB with either WDR5-GFP or GFP-HP1α, we observed distinct behaviors. HP1α readily partitioned into ISB condensates and formed fully mixed droplets[28] (Fig. 2e, top, f). Interestingly, droplets of WDR5 and ISB did not completely mix but instead formed a concentric bilayer structure in which ISB enveloped WDR5 (Fig. 2e, bottom, g). To quantify this behavior, mixed droplets were classified as either fully mixed or concentric bilayer structures based on their fluorescence distribution patterns. WDR5–ISB mixtures were strongly enriched for concentric bilayer droplets, whereas HP1α–ISB mixtures were predominantly fully mixed (Fig. 2h). WDR5-GFP and mCherry-HP1α also displayed clear immiscibility (Supplementary Fig. 5a, b). Moreover, WDR5–ISB immiscibility persisted over time, in the presence of nuclear extract, and across a range of salt concentrations (Supplementary Fig. 5c–f). These results indicate that WDR5 and ISB form robustly immiscible architectures under the tested conditions. To explore the physical basis of this behavior, we next established a simulation framework.

Repulsion governs WDR5-ISB immiscibility

We modeled the dynamics of WDR5 and ISB using the Cahn–Hilliard equation, coupled with a Flory–Huggins free energy scheme[40]. Three interaction parameters were considered: χ_{ws}, describing WDR5–solvent interactions; χ_{cs}, describing ISB–solvent interactions; and χ_{wc}, describing WDR5–ISB interactions. Higher χ values correspond to greater energetic penalties in the mixed state and thus stronger tendencies toward phase separation[41]. To determine the relationship among these parameters, we performed systematic simulations over their combined ranges (Supplementary Figs. 6 and 7).

The experimentally observed bilayer structure failed to form when either WDR5 or ISB lacked LLPS capability, indicating that phase separation of both components is required for immiscible droplet assembly (Supplementary Fig. 8a). Even when both components retained LLPS propensity ($\chi_{ws} > 0$, $\chi_{cs} > 0$), setting $\chi_{wc} = 0$ did not generate a bilayer structure, showing that WDR5–ISB repulsion is also required (Fig. 2i, top, Supplementary Fig. 6a, and Supplementary

https://doi.org/10.1038/s41467-026-74446-6

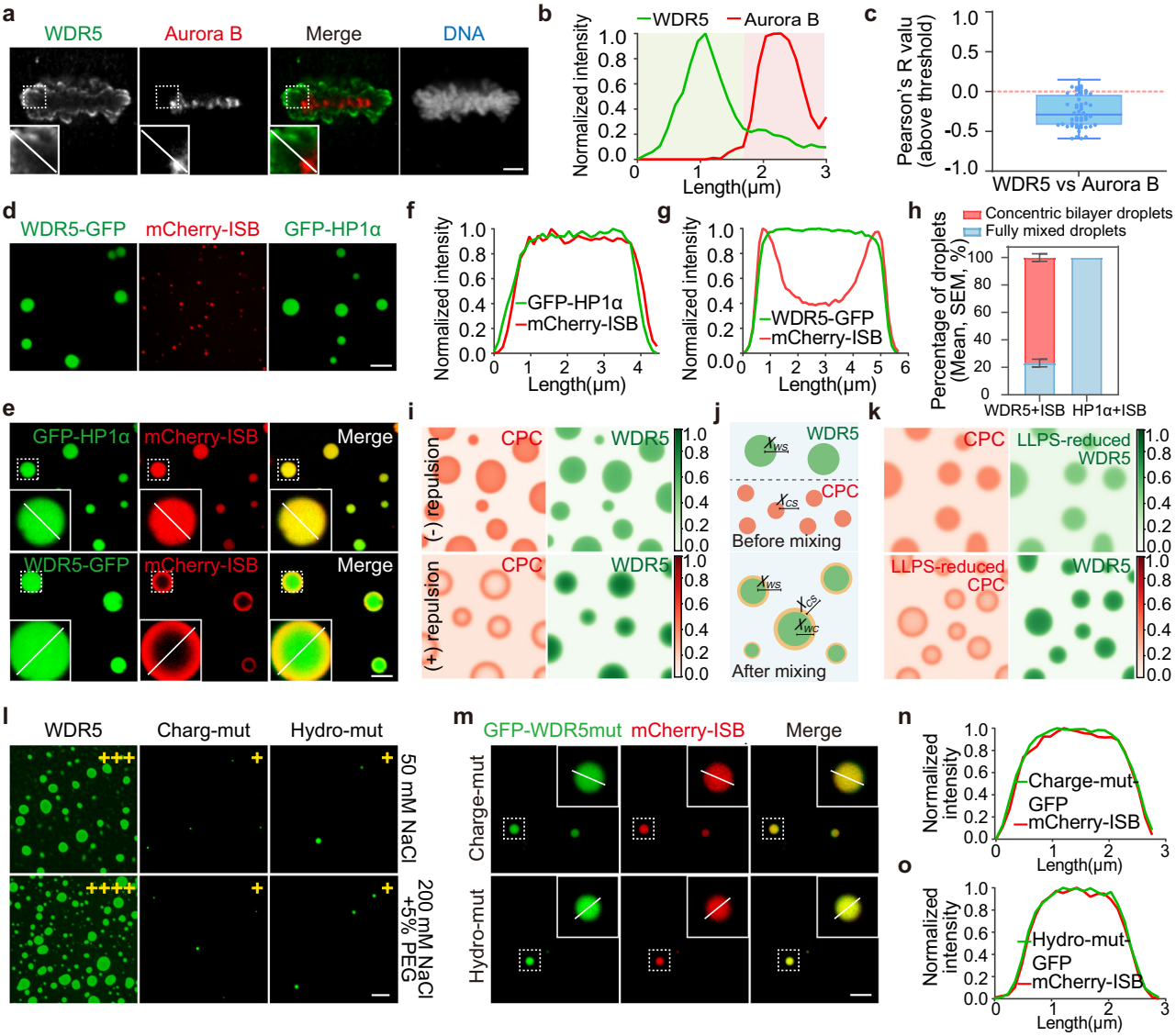

Fig. 2 | LLPS-driven repulsion promotes immiscibility between WDR5 and CPC condensates. a Immunofluorescence images of HeLa cells co-stained for WDR5 (green), Aurora B (red), and DNA (blue), representative of three independent experiments. **b** Line-scan profiles of WDR5 and Aurora B across the magnified region in (**a**) (2.3-fold enlargement). Shaded areas indicate signal distributions. **c** Quantification of above-threshold Pearson's correlation coefficients between WDR5 and Aurora B. $n = 50$ cells. Box plots show the median, 25th and 75th percentiles, and minimum and maximum values; points represent cells. The red dashed line indicates $r = 0$. **d** Condensates formed by WDR5-GFP, mCherry-ISB, and GFP-HP1α in a buffer containing 125 mM NaCl and 10% PEG8000. Protein concentration, 10 μM. Images are representative of three independent experiments. **e** Two-color droplet-mixing assays performed under the same conditions as in (**d**). **f** Line-scan analysis of the boxed droplet HP1α/ISB droplet region in (**e**) (threefold enlargement). **g** Line-scan analysis of the boxed WDR5/ISB droplet region in (**e**) (threefold enlargement). **h** Quantification of concentric bilayer or fully mixed droplets according to fluorescence distribution patterns. $n = 21$ droplets per group. **i** Simulation snapshots showing WDR5 and CPC distributions with $\chi_{ws} = 4.5, \chi_{cs} = 3.5$ and $\chi_{wc} = 0$ or $\chi_{wc} = 3.0$, as indicated. **j** Schematic of parameter regimes governing WDR5-CPC droplet organization. Bar lengths represent interaction parameter strengths. **k** Simulations under two parameter sets: $\chi_{ws} = 3.0, \chi_{cs} = 3.5, \chi_{wc} = 1.5$ and $\chi_{ws} = 4.5, \chi_{cs} = 2.3, \chi_{wc} = 1.5$, as indicated. "LLPS-reduced" indicates reduced liquid-liquid phase separation (LLPS) propensity. **l** Condensates formed by GFP-tagged WDR5, Charge-mut and Hydro-mut. Protein concentration, 30 μM. "Charge-mut" and "Hydro-mut" denote WDR5 mutants affecting positively charged and hydrophobic residues, respectively. Images are representative of three independent experiments. **m** Representative images and line-scan analyses of binary droplets formed by Charge-mut or Hydro-mut with ISB under the same conditions as in (**d**). "WDR5mut-GFP" denotes Charge-mut and Hydro-mut. **n** Line-scan analysis of the boxed Charge-mut/ISB droplet region in (**m**) (threefold enlargement). **o** Line-scan analysis of the boxed Hydro-mut/ISB droplet region in (**m**) (threefold enlargement). Scale bars, 5 μm.

Movie 1). With moderate $\chi_{wc} > 0$, the relative magnitudes of χ_{ws} and χ_{cs} determined whether a bilayer formed and which phase occupied the outer layer (Supplementary Fig. 6b). At higher χ_{wc} values, dumbbell-like morphologies emerged instead (Supplementary Fig. 6c). Based on these results and prior theoretical work[41,42], we conclude that the parameters must satisfy $\chi_{ws} > \chi_{cs} > \chi_{wc} > 0$ to produce a bilayer with CPC outside and WDR5 inside (Fig. 2i, bottom and Supplementary Movie 2). The simulated concentration profile across the bilayer interface closely matched the experimental fluorescence distribution (Fig. 2g and Supplementary Fig. 8e, f). A summary of the physical meanings of these interaction parameters is shown in Fig. 2j.

We next asked how this bilayer architecture could be disrupted. Because WDR5 is broadly distributed along chromosome arms, whereas CPC is confined to centromeres, we reasoned that WDR5 is likely present at higher abundance than CPC. We therefore varied the WDR5:CPC stoichiometry from 1:1 to 5:1. Across all tested ratios,

selectively reducing WDR5 LLPS propensity by lowering χ_{ws} was insufficient to abolish the bilayer structure (Supplementary Fig. 8b). Since repulsive forces between these condensates are prerequisites for immiscibility[42–44], we next co-reduced χ_{ws} and χ_{wc}, which led to complete mixing (Fig. 2k, top and Supplementary Fig. 8c), whose concentration profile again matched the experimental distribution (Supplementary Fig. 8e, g). In contrast, equivalent co-reduction of χ_{cs} and χ_{wc} had little effect on bilayer integrity (Fig. 2k, bottom), and the bilayer persisted even upon further suppression of χ_{cs} (Supplementary Fig. 8d). These results indicate that WDR5-driven phase separation, together with repulsive WDR5–ISB interactions, is the dominant determinant of bilayer immiscibility.

To validate these findings experimentally, we generated WDR5 mutants with altered charged or hydrophobic residues within its IDR. In vitro assays demonstrated that these mutations significantly reduced the LLPS propensity of WDR5 (Fig. 2l). Intriguingly, when ISB was mixed with these WDR5 mutants, the fusion of WDR5 and ISB droplets occurred (Fig. 2m–o), suggesting that these mutations synergistically reduced both LLPS propensity and repulsive forces. This indicates that positively charged and hydrophobic amino acids within the IDR of WDR5 are crucial for generating repulsive forces between WDR5 and CPC condensates.

These findings highlight the critical role of repulsive forces between WDR5 and CPC droplets in preventing their complete fusion. Notably, WDR5-driven LLPS dominates this process, and the key amino acids required for WDR5 LLPS are also essential for generating repulsive forces against CPC. This suggests fundamental principles governing the exclusive interactions between WDR5 and CPC, which likely drive their compartmentalized distribution on chromosomes in mitotic cells.

LLPS-deficient WDR5 disrupts compartments

WDR5 binds to the histone H3 tail[45] and is recruited to chromatin as an H3R2 symmetric dimethylation (H3R2me2s)[46] and H3Q5 serotonylation (H3Q5ser)[47] reader protein, whereas phosphorylated H3T3 recruits CPC to centromeres[19–21]. Based on these recruitment factors, we incorporated a potential energy field[48] into our simulation model, defining CPC recruitment sites at centromeres and WDR5 recruitment on chromosome arms. The simulations successfully recapitulated the distinct localization patterns of WDR5 and CPC on chromosomes (Fig. 3a, left panel, Supplementary Fig. 9a, and Supplementary Movie 3). When CPC recruitment sites were removed, CPC failed to accumulate at centromeres, despite maintaining LLPS propensity (Supplementary Fig. 9b). Similarly, deleting WDR5 recruitment sites reduced WDR5 levels on chromosome arms, leading to diffuse CPC localization around centromeres (Supplementary Fig. 9c). Notably, reducing the LLPS propensity of WDR5 disrupted the compartmentalized segregation of WDR5 and CPC, resulting in diffuse distributions of both proteins (Fig. 3a, middle panel). In contrast, reducing the LLPS propensity of CPC had only a minor effect on their segregation (Fig. 3a, right panel). These simulation data suggest that phase separation, particularly of WDR5, and histone modification recruitment synergistically determine the compartmentalized localization of WDR5 and CPC on chromosomes, with LLPS propensity likely dominating interaction behaviors between these membraneless regions.

To test these predictions experimentally, we introduced siRNA-resistant Flag-tagged wild-type WDR5 (Flag-WDR5) or LLPS-deficient mutant (WDR5-ΔIDR) into WDR5-depletion cells and assessed their functionality via IF assays. Wild-type WDR5 restored the centromeric enrichment of Aurora B, whereas WDR5-ΔIDR failed to do so, resulting in Aurora B spreading along chromosome arms and persistent chromosome misalignment (Fig. 3b, e). Consistent with this defect, ectopic H3T3ph on chromosome arms remained elevated in WDR5-ΔIDR-rescued cells, while H3K4me3 levels were lower than those of the control (Fig. 3c, d, f). These results indicate that LLPS-deficient WDR5 is unable to re-establish the compartmentalized distribution of chromosomal histone modifications required for proper Aurora B localization. In line with this conclusion, additional WDR5 mutants that impair LLPS, including charge- and hydrophobicity-defective variants, also failed to restore Aurora B localization (Supplementary Fig. 10).

To further dissect the relative contributions of chromatin binding and LLPS function, we fused either siRNA-resistant wild-type WDR5 or WDR5-ΔIDR to the chromatin-targeting domain H2B, generating Flag-H2B-WDR5 and Flag-H2B-WDR5-ΔIDR. Flag-H2B-WDR5 successfully rescued Aurora B localization in WDR5-depleted cells, whereas Flag-H2B-WDR5-ΔIDR, despite being efficiently tethered to chromosomes, failed to restore centromeric Aurora B enrichment (Fig. 3b, e). Consistently, chromatin anchoring of WDR5-ΔIDR did not re-establish the spatial segregation of H3T3ph and H3K4me3 (Fig. 3c, d, f). Thus, chromatin association alone is insufficient to recapitulate WDR5 function, whereas LLPS capacity is required for proper chromosomal compartmentalization and CPC positioning.

We further examined another CPC component, Survivin, using the same rescue strategy. Similar to Aurora B, both siRNA-resistant wild-type WDR5 and H2B-WDR5 restored centromeric Survivin localization in WDR5-depleted cells, whereas WDR5-ΔIDR and H2B-WDR5-ΔIDR failed to rescue its localization intensity (Supplementary Fig. 11). Together, these results support the conclusion that WDR5 LLPS, rather than chromatin binding alone, is required for proper CPC confinement on mitotic chromosomes.

Compartmentalization requires LLPS-mediated repulsion

Chromosomal deposition of WDR5 relies on its LLPS behavior. Our results indicate that reduced WDR5 LLPS not only weakens repulsive forces between WDR5 and CPC condensates but also decreases H3K4me3 levels. To further elucidate the contributions of repulsive force-mediated compression and H3K4me3-mediated inhibition of H3T3ph in establishing epigenetic compartments, strategies to restore H3K4me3 levels independently of repulsive forces are necessary. To address this, we devised a targeted rescue strategy by fusing MLL1 fragments[49] or Menin, which are involved in H3K4 methylation, with H2B. This approach specifically restored H3K4me3 levels without reconstituting WDR5 LLPS-mediated repulsive forces. Among these constructs, H2B-MLL1-TAD most effectively restored global H3K4me3 levels in WDR5-depleted cells (Fig. 4a, c, left panel) and substantially recovered its chromosomal distribution pattern (Fig. 4d), whereas the other fusion proteins showed only partial rescue (Supplementary Fig. 12a, b). We therefore selected H2B-MLL1-TAD for subsequent analyses.

Despite the restoration of H3K4me3, Aurora B localization was not rescued (Fig. 4c, right panel and Supplementary Fig. 12c). Consistently, expression of an MLL1-TAD fragment without the H2B tag also restored H3K4me3 levels in WDR5-depleted cells, but still failed to recover Aurora B localization (Supplementary Fig. 12d, e). We next examined the effect of H2B-MLL1-TAD on H3T3ph distribution in WDR5-depleted cells. Restoring H3K4me3 suppressed the ectopic hyperphosphorylation of H3T3ph on chromosome arms (Fig. 4b, e, left panel), but did not re-establish its centromeric confinement. Instead, H3T3ph remained elevated along chromosomes and reduced at centromeres relative to controls (Fig. 4e). Furthermore, centromeric enrichment of Aurora B was not restored, and Aurora B remained redistributed along chromosome arms (Fig. 4f).

These results indicate that H3K4 methylation alone is insufficient to rebuild the spatial organization of the H3T3ph/CPC module. Although restoration of H3K4me3 attenuated the arm-biased increase in H3T3ph, it failed to re-establish the precise centromeric confinement of H3T3ph and Aurora B. Together, these data demonstrate that LLPS-mediated repulsion, rather than H3K4 methylation alone, is

https://doi.org/10.1038/s41467-026-74446-6

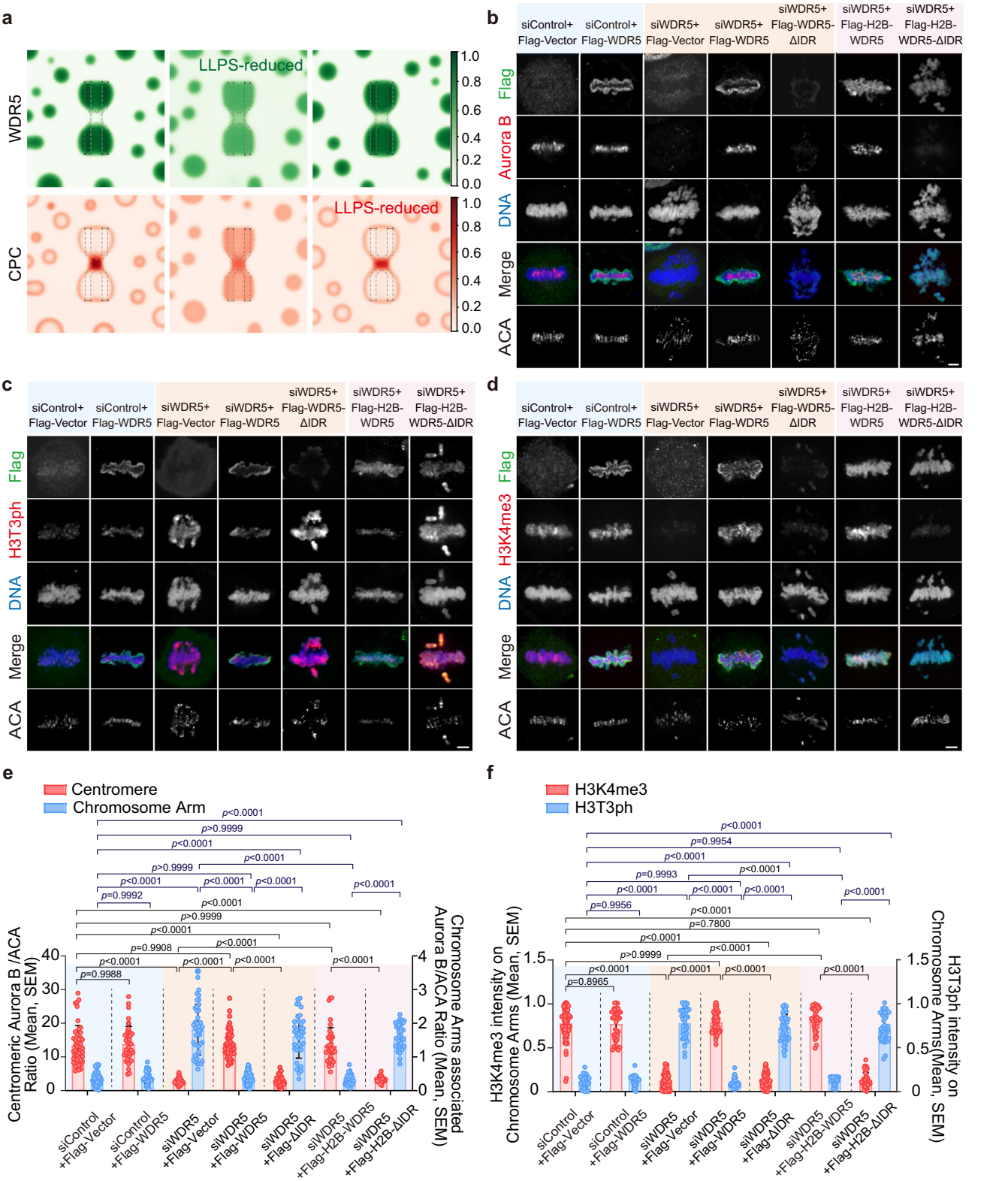

Fig. 3 | LLPS-deficient WDR5 mutants fail to re-establish distinct H3T3ph and H3K4me3 compartments and Aurora B localization. a Representative simulation snapshots showing WDR5 and CPC distributions on chromosomes under different parameter settings, using the interaction parameters from Fig. 2i, k, as indicated. **b** HeLa cells were treated with control siRNA or WDR5 siRNA, transfected with the indicated plasmids, treated with monastrol, released by washout, and subsequently treated with MG132. Cells were stained for Flag (green), Aurora B (red), and DNA (blue). **c** HeLa cells were processed as in (**b**) and stained for Flag (green), H3T3ph (red), and DNA (blue). **d** HeLa cells were processed as in (**b**) and stained for Flag (green), H3K4me3 (red), and DNA (blue). **e** Quantification of Aurora B fluorescence intensity at centromeres and on chromosome arms, relative to ACA. $n = 46$, 40, 42, 48, 38, 40, and 35 cells for the indicated groups from three independent experiments. **f** Quantification of H3T3ph and H3K4me3 fluorescence intensities on chromosome arms. For H3K4me3, $n = 88$, 40, 84, 79, 62, 40, and 50 cells; for H3T3ph, $n = 49$, 41, 49, 40, 42, 41, and 42 cells for the indicated groups from three independent experiments. Statistical significance in (**e**, **f**) was determined by one-way ANOVA followed by Tukey's multiple-comparison test. Images in (**b**–**d**) are representative of three independent experiments with similar results. Scale bars, 5 µm.

https://doi.org/10.1038/s41467-026-74446-6

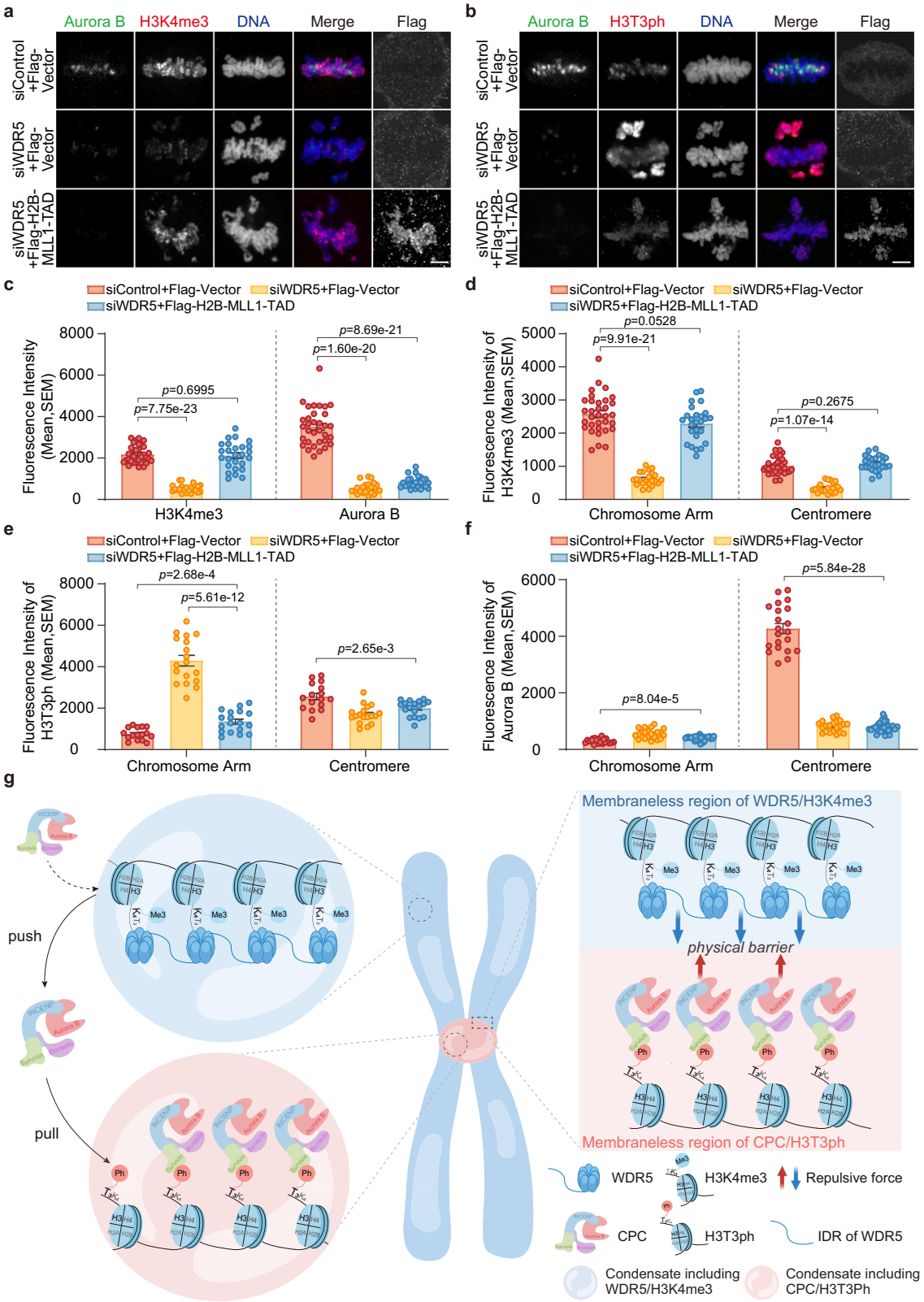

essential for CPC confinement and epigenetic compartmentalization on mitotic chromosomes.

Perturbation of WDR5 condensates mislocalizes Aurora B

To further test whether disruption of WDR5 condensates is sufficient to perturb CPC positioning, we sought a selective means to interfere with WDR5 phase separation. The WIN (WDR5 interaction) site binds proteins containing a WIN motif[50], and notably, the N-terminal IDR of WDR5 itself contains a WIN motif within its arginine-rich region, raising the possibility that this motif contributes to WDR5 self-association and condensate formation. We therefore screened a series of WIN-derived peptides using in vitro LLPS assays and identified ARAQ as the most effective peptide in disrupting WDR5 droplet formation (Supplementary Fig. 13a, b). Importantly, these peptides did not perturb ISB

Fig. 4 | Repulsion-driven compartmentalization and epigenetic-mediated recruitment synergistically ensure Aurora B centromere fidelity. a HeLa cells were treated with control siRNA or WDR5 siRNA, transfected with the indicated plasmids, treated with monastrol, released by washout, and subsequently treated with MG132. Cells were stained for Aurora B (green), H3K4me3 (red), and DNA (blue). **b** HeLa cells were processed as in (**a**) and stained for Aurora B (green), H3T3ph (red), and DNA (blue). **c** Quantification of H3K4me3 and Aurora B fluorescence intensities. $n = 33$, 22, 26 cells. **d** Quantification of H3K4me3 fluorescence intensity on chromosome arms and at centromeres. $n = 33$, 22, and 26 cells. **e** Quantification of H3T3ph fluorescence intensity on chromosome arms and at centromeres. $n = 16$, 18, and 18 cells. **f** Quantification of Aurora B fluorescence intensity on chromosome arms and at centromeres. $n = 21$, 21, and 30 cells. Statistical significance in (**d**–**f**) was determined by two-tailed unpaired Student's t test. **g** Model for phase separation-driven compartmentalization on mitotic chromosomes. WDR5/H3K4me3 condensates exclude CPC from chromosome arms, whereas centromeric H3T3ph recruits CPC. These repulsive and recruitment-based mechanisms promote spatial segregation between chromosome-arm and centromeric domains, thereby supporting Aurora B enrichment at functional centromeres.

condensates (Supplementary Fig. 13c, d), indicating target selectivity. In cells, ARAQ treatment disrupted WDR5 chromosomal localization during mitosis (Supplementary Fig. 13e), abolished centromeric Aurora B accumulation, and induced chromosome misalignment (Supplementary Fig. 13f, g). Together, these findings provide independent evidence that the integrity of WDR5 condensates is required for proper CPC confinement and chromosome alignment.

Discussion

Our study supports a model in which mitotic chromosome organization emerges from the interplay between biochemical recruitment and biophysical exclusion. We show that the N-terminal IDR of WDR5 promotes phase separation and enables WDR5 condensates to remain immiscible with CPC condensates. This phase-based repulsion establishes a physical barrier that partitions H3K4me3-enriched chromosome arms from H3T3ph-rich centromeric domains (Fig. 4g, right panel). The underlying regulatory principle combines a biochemical pull via H3T3ph-mediated CPC recruitment and a biophysical push via LLPS-driven immiscibility between WDR5 and CPC condensates (Fig. 4g, left panel). This dual mechanism offers a framework for how broadly distributed enzymatic activities can generate spatially confined epigenetic patterns and selectively position downstream effectors.

Beyond its canonical role as a methyltransferase scaffold[32,33], WDR5 emerges here as an active organizer of chromatin domains through phase-mediated repulsion. Notably, restoring H3K4me3 levels alone in WDR5-deficient cells fails to rescue Aurora B localization or proper chromosome alignment, underscoring that LLPS-based exclusion, rather than epigenetic marks, is critical for spatial specificity within mitotic chromosome compartments. This repulsion-based distribution mechanism may extend beyond mitosis to other contexts requiring spatial precision, such as the segregation of transcriptionally active and repressive domains or the exclusion of DNA repair foci from transcriptional condensates— scenarios likely governed by analogous phase immiscibility between distinct chromatin states[27].

Our study also establishes the IDR of WDR5 as a critical determinant of chromosomal compartmentalization. This disordered region encodes the biophysical properties required for phase separation and spatial exclusion. Disruption of WDR5 condensates, via IDR deletion or IDR-targeted peptides, disperses H3T3ph patterns and mislocalizes Aurora B, suggesting that modulating disordered regions to alter condensate properties could offer a viable strategy for targeting chromatin-associated regulators in disease contexts.

Furthermore, we show that WDR5 preferentially localizes to chromosome arms through phase separation (Fig.1a, b), regions composed of condensed euchromatin that support gene expression. This spatial positioning provides a foundation for WDR5-driven gene reactivation during mitotic exit[36]. At the interface where WDR5 and CPC condensates repel each other, spatial proximity permits MLL1/WDR5-mediated methylation of Borealin[30], facilitating CPC condensate formation. This interaction may contribute to the establishment of a stable, mutually exclusive system between WDR5 and CPC, which guides functionally distinct and domain-specific chromatin organization.

Several limitations should be considered. First, the spatial relationship between centromeric and pericentromeric regions was assessed mainly by diffraction-limited fluorescence imaging, which cannot fully resolve domain boundaries. Second, our simulation framework is coarse-grained and is intended to define a physical regime compatible with the observed architectures rather than provide a complete molecular description of the in vivo system. Third, although our temporal analyses and rescue experiments argue against a purely indirect transcriptional explanation, secondary effects associated with siRNA depletion cannot be excluded completely. Finally, the molecular basis of the repulsive interaction between WDR5 and CPC condensates remains to be defined. Addressing these questions with acute perturbation strategies, higher-resolution imaging, and more detailed biophysical reconstitution will help refine the model proposed here.

In summary, our study reveals that eukaryotic cells integrate LLPS-driven repulsion with epigenetic marks to achieve high-fidelity mitotic chromosome segregation, a finding that has general implications for understanding functions of biomolecules in cells and for organizing higher-order genome compartmentalization. Future exploration of phase immiscibility across diverse chromatin states will delineate how cells encode spatiotemporal information without membranous boundaries.

Methods

Bacterial strain

Escherichia coli BL21-(DE3)-RIPL cells (Tsingke) were used in this study to express all the recombinant proteins. Transfected cells were cultured in LB medium supplemented with necessary antibiotics at 37 °C with 220 rpm shaking and expressed at 16 °C with 220 rpm shaking.

DH5α (Tsingke) were used to generate plasmids. Cells were cultured in LB medium supplemented with necessary antibiotics at 37 °C with 220 rpm shaking.

Cell lines

HeLa and COS-7 cells were obtained from the Cell Bank of the Chinese Academy of Sciences and cultured in Dulbecco's Modified Eagle Medium (DMEM, Thermo Fisher Scientific, #11995065) supplemented with 10% fetal bovine serum (FBS, Thermo Fisher Scientific, #10099-141), 1% penicillin–streptomycin (VivaCell, #C3420-0100) and maintained at 37 °C under 5% CO_2.

Cell transfection and synchronization

HeLa cells were cultured in high-glucose DMEM supplemented with 10% fetal bovine serum and 1% penicillin–streptomycin at 37 °C in a humidified atmosphere with 5% CO_2. For transfection, plasmid DNA was introduced using Lipofectamine 3000 (Thermo Fisher Scientific), and siRNA transfection was performed using siRNA-Mate (GenePharma), following the manufacturer's instructions. The siRNA oligonucleotide sequence targeting WDR5 was 5′-GAUGGAUCCUUGAUAGUUU-3′ (synthesized by GenePharma)[51].

To synchronize HeLa cells at the G1/S transition, cells were treated with 2.5 mM thymidine (Sigma-Aldrich, M1404) for 18–20 h and subsequently released by washing with PBS. For specific experiments, cells were treated with 100 μM Eg5 inhibitor monastrol (MCE, HY-101071A)

for 2 h, 20 μM proteasome inhibitor MG132 (MCE, HY-13259C) for 1 h, or 100 ng/mL microtubule inhibitor nocodazole (Sigma-Aldrich, M1404) for 1 h[17,20,52]. For the monastrol washout assay, cells were treated with monastrol for 2 h, followed by three washes with PBS, and then treated with MG132 for 1 h.

Genes and plasmids

The cDNA encoding human WDR5 (residues 1–332) was cloned into the pEGFP-N1 vector to generate a C-terminal EGFP-tagged construct (WDR5-GFP). For rescue experiments, an siRNA-resistant version of WDR5 (residues 1–332) was cloned into the p3xFLAG-Myc-CMV-24 vector to generate an N-terminal 3×Flag-tagged construct (Flag-WDR5). Silent mutations were introduced into the siRNA target region to generate the siRNA-resistant WDR5 construct. The N-terminal intrinsically disordered region (IDR) of WDR5 used in this study corresponds to residues 1–32 and has the sequence MATEEKKPETEAAR-AQPTPSSSATQSKPTPVK. A truncated variant lacking this region (residues 33–332) was generated in both backbones, yielding WDR5-ΔIDR-GFP and Flag-WDR5-ΔIDR.

To assess the contribution of the IDR sequence, two mutant series were generated within residues 1–32. In the charge mutant, positively charged residues were replaced with alanine (K6A, K7A, R14A, K27A, K32A; Flag-Charge-mut). In the hydrophobic mutant, hydrophobic residues were replaced with glycine (A2G, A12G, A13G, A15G, A23G, V31G; Flag-Hydro-mut). To test the contribution of chromatin tethering, the H2B domain was inserted into the corresponding Flag-tagged constructs to generate Flag-H2B-WDR5, Flag-H2B-WDR5-ΔIDR, Flag-H2B-Charge-mut, and Flag-H2B-Hydro-mut.

To restore intracellular levels of H3K4 trimethylation (H3K4me3), truncated cDNA fragments of MLL1 were cloned into the Flag-H2B vector[49]. These included MLL1-C (residues 2720–3969), MLL1-TAD (residues 2846–3969), MLL1-FYRC (residues 3665–3969), MLL1-SET (residues 3762–3969), as well as the cDNA encoding Menin (residues 1–610). The resulting plasmids were Flag-H2B-MLL1-C, Flag-H2B-MLL1-TAD, Flag-H2B-MLL1-FYRC, Flag-H2B-MLL1-SET, and Flag-H2B-Menin. In addition, a construct lacking the H2B tag was generated for MLL1-TAD (Flag-MLL1-TAD).

For optoDroplet experiments, cDNAs encoding WDR5 (residues 1–332) and WDR5-ΔIDR (residues 33–332) were cloned into the mCherry-CRY2PHR vector, generating WDR5-mCherry-CRY2PHR and WDR5-ΔIDR-mCherry-CRY2PHR, respectively. To generate the IDR replacement construct, the endogenous WDR5 IDR was replaced by the Pub1 IDR (residues 243–327), which was fused to the N-terminus of WDR5-ΔIDR in the same backbone, yielding Pub1_IDR-WDR5-ΔIDR-mCherry-CRY2PHR.

Antibodies

The following antibodies were used in this study: WDR5 (sc-393080, 1:100 dilution for immunofluorescence staining [IF], 1:500 dilution for Western blot [WB]), H3 (sc-517576, 1:500 dilution for WB), and Cyclin B1 (sc-245, 1:500 dilution for WB), all purchased from Santa Cruz Biotechnology. Aurora B (ab2254, 1:1000 dilution for IF, 1:1000 dilution for WB) antibody was purchased from Abcam. H3T3ph (D5G1I, 1:3200 dilution for IF, 1:1000 dilution for WB), H3K4me3 (C42D8, 1:300 dilution for IF, 1:1000 dilution for WB), Survivin (71G4B7, 1:500 dilution for IF), and Phospho-CENP-A (2187, 1:100 dilution for IF, 1:1000 dilution for WB) antibodies were obtained from Cell Signaling Technology. The Flag antibody (F1804, 1:100 dilution for IF) was purchased from Sigma-Aldrich, and the Centromere antibody (HCT-0100, 1:2500 dilution for IF) was purchased from ImmunoVision.

Live-cell imaging

For live imaging of WDR5-GFP and WDR5-ΔIDR-GFP protein localization in mitotic HeLa cells, cells were plated onto 18 × 18 mm glass coverslips pre-coated with Poly-D-lysine (Sigma-Aldrich, P6407). The coverslips were subsequently mounted in custom-designed Rose chambers with L-15 medium lacking phenol red (Gibco, 21083027). Temperature was maintained between 35 and 37 °C using a laboratory-constructed temperature control system.

Imaging was performed on a Nikon ECLIPSE Ti confocal microscope, equipped with a ×100 1.4 NA objective, an XY-piezo Z stage (Applied Scientific Instrumentation), a Yokogawa spinning disk confocal unit, an Andor electron multiplier CCD camera, and an Andor LMM5 laser merge module, all controlled by Andor iQ3 software. Images were acquired with a 0.5-μm z-spacing, typically capturing 3–5 optical planes.

Immunofluorescence staining

HeLa cells were seeded onto 20 × 20 mm glass coverslips pre-coated with poly-D-lysine (Sigma-Aldrich, P6407). Cells were fixed in 4% paraformaldehyde for 10 min and permeabilized in PBS containing either 0.1% Triton X-100 for Supplementary Fig. 1b or 0.4% Triton X-100 for all other immunofluorescence experiments for 10 min. Blocking was performed with PBS containing 1% BSA and 0.1% Tween-20 for 30 minutes at room temperature. For immunostaining, cells were incubated with primary antibodies overnight at 4 °C, followed by incubation with the corresponding secondary antibodies at room temperature for 1 h.

For multiplex labeling of primary antibodies from identical host species, the FlexAble direct labeling kit (Proteintech) was used according to the manufacturer's protocol, enabling covalent conjugation of spectrally distinct fluorophores to primary antibodies via FlexLinker® technology. Images were analyzed using ImageJ.

Colocalization analysis

Co-stained fluorescence images of WDR5–Aurora B, H3T3ph–H3K4me3, and H3K4me3–Aurora B were analyzed on a per-cell basis in Fiji (ImageJ) using the Coloc2 plugin. Images were split into individual channels and cropped to single cells. The region of interest (ROI) was defined as the whole-cell area. Costes automatic thresholding was applied independently to each channel, and Pearson's correlation coefficient above threshold (PCC^AT) was calculated using only pixels above the respective thresholds to reduce background-driven correlations. The reported values represent Pearson's R above threshold.

Protein expression and purification

The coding sequences for human WDR5 (wild-type, truncated, and mutant variants) were cloned into the pET28a vector, which was then fused with a C-terminal mEGFP. The full-length coding sequence for HP1α was cloned into the pHis-mEGFP vector[53], resulting in an N-terminal 6×His and mEGFP tag fusion. For mCherry-ISB[28], the coding sequences for Survivin and Borealin were cloned into the pET28a vector, with mCherry inserted between the 6×His tag and INCENP (1–58), creating the 6×His-mCherry-ISB construct.

Proteins including WDR5-GFP, WDR5-ΔIDR (33–334)-GFP, WDR5-Charge-mut-GFP, and WDR5-Hydro-mut-GFP were expressed in *Escherichia coli* BL21 (DE3) cells. Cells were cultured in Luria-Bertani medium containing 50 μg/mL kanamycin at 37 °C until the optical density (OD600) reached approximately 0.8–1.0. Protein expression was induced with 0.5 mM isopropyl β-D-thiogalactopyranoside (IPTG) for 18–22 h at 16 °C. After induction, cells were harvested by centrifugation at 4 °C at 5000 rpm for 15 minutes. The cell pellets were resuspended and lysed in buffer A (1 M NaCl, 20 mM Tris-HCl, pH 8.0), followed by sonication. The lysates were then centrifuged at 13,000 rpm for 30 minutes at 4 °C. The supernatants were loaded onto a Ni^{2+}-chelating resin (GE Healthcare) for affinity chromatography. After washing with buffer B (1 M NaCl, 20 mM Tris-HCl, pH 8.0, 30 mM imidazole) to remove impurities, the proteins were eluted using pre-chilled buffer C (1 M NaCl, 20 mM Tris-HCl, pH 8.0, 500 mM

imidazole). The eluted proteins were further purified via size-exclusion chromatography on a HiLoad 16/600 Superdex 200 column (GE Healthcare) in buffer D (500 mM NaCl, 20 mM Tris-HCl, pH 8.0, 1 mM DTT). The desired protein fractions were collected and concentrated using Amicon Ultra-15 Centrifugal Filters (10 K MWCO, Millipore).

The GFP protein was similarly expressed in *E. coli* BL21 (DE3) cells and purified as described above. The GFP-HP1α protein and the mCherry-ISB protein complexes were purified according to previously established protocols[28,53]. All purified proteins were stored at −80 °C.

In vitro phase separation assay

Purified proteins were concentrated and desalted to an appropriate protein concentration using Amicon Ultra centrifugal filters (10 KMWCO, Millipore). The proteins were then added to droplet formation buffer, which consisted of either 125 mM NaCl, 20 mM Tris-HCl (pH 8.0), 1 mM Dithiothreitol (DTT), and 10% PEG8000, or 200 mM NaCl, 20 mM Tris-HCl (pH 8.0), 1 mM DTT, and 5% PEG3350[28,37,54]. In the two-color droplet mixing assay, proteins were individually induced to form droplets under the conditions of 125 mM NaCl, 20 mM Tris-HCl (pH 8.0), 1 mM DTT, and 10% PEG8000, and were then mixed together, followed by immediate observation of droplet interactions under the microscope.

For in vitro droplet assays, phase-separated droplets were defined operationally as microscopically visible, approximately spherical condensates that were distinguishable from the surrounding dilute phase. Droplet classification was based on morphology and liquid-like behavior, rather than on a fixed size threshold.

Preparation of nuclear extracts (NE)

HeLa cells were harvested at a certain density by centrifugation at 3000 rpm for 10 minutes. The cell pellets were washed twice with PBS and resuspended in ice-cold NE buffer I [0.3 M sucrose, 60 mM KCl, 15 mM NaCl, 5 mM $MgCl_2$, 0.1 mM EGTA, 15 mM Tris-HCL (pH 7.5), 0.5 mM DTT, 0.1 mM PMSF, 10 mM Sodium butyrate, and protease inhibitors]. An equal volume of ice-cold NE buffer I containing 0.4% NP-40 (NonidetP-40) was added. Mix gently and incubate on ice for 5 minutes. Then, 8 volumes of ice-cold Hypertonic sucrose buffer (NE buffer II) [1.2 M sucrose, 60 mM KCl, 15 mM NaCl, 5 mM $MgCl_2$, 0.1 mM EGTA, 15 mM Tris-HCl (pH 7.5), 0.5 mM DTT, 0.1 mM PMSF, 10 mM Sodium butyrate, and protease inhibitors] were added to the centrifuge tube. The cell suspension was carefully layered onto the surface of NE buffer II and centrifuged at 10,000× g for 20 min at 4 °C. Following centrifugation, a stratified suspension was observed. The upper layer, containing NP-40, was carefully removed with a pipette, changing the tip between samples to avoid cross-contamination. The second layer of supernatant was then discarded, and the pellet was resuspended in ice-cold Micrococcal Nuclease Reaction Buffer supplemented with Micrococcal Nuclease (NEB, M0247S), according to the manufacturer's instructions for digestion. The digestion reaction was terminated by adding 10 mM EGTA, and the mixture was centrifuged at 13,000 rpm for 20 min at 4 °C. The resulting supernatant, containing the nuclear extract, was analyzed by 0.5% agarose gel electrophoresis for confirmation.

Fluorescence recovery after photobleaching (FRAP)

Images were acquired using a Nikon A1R HD25 confocal microscope. For the in vitro assay, droplets formed by recombinant WDR5-GFP protein and by the interaction of WDR5-GFP with NE were excited with 488-nm laser light. For the in vivo assay, WDR5-GFP expressed in chromosome-localized regions of HeLa cells was similarly excited with 488-nm laser light. To assess condensate dynamics, the fluorescence intensity of the condensates was bleached by at least 50%, and fluorescence recovery was monitored at 1-s intervals. Fluorescence intensity at the bleached region was quantified using the FIJI plugin FRAP Profiler V2. Data were processed, and recovery curves were generated using GraphPad Prism 10.4.0.

Western blotting

Proteins were separated by SDS-PAGE and transferred to PVDF membranes (Millipore, IPVH00010). The membranes were incubated overnight at 4 °C with specific primary antibodies, followed by incubation with horseradish peroxidase (HRP)-conjugated secondary antibodies. Protein bands were visualized using a UVP Gel Imaging System (BioDoc-It220) following chemiluminescent detection.

Synthesis and treatment of peptides

The peptides used in this study, including EAARAQP, AARAQ, AARA, and ARAQ, were synthesized by Genscript (Nanjing, China) with a purity of ≥95%. All peptides were dissolved in dimethyl sulfoxide (DMSO) to prepare stock solutions at the desired concentrations. Peptide stock solutions were aliquoted and stored at −80 °C to avoid repeated freeze–thaw cycles. Before use, the peptides were thawed and diluted in culture medium or assay buffer as required for individual experiments. For cellular assays, HeLa cells were treated with 20 μM ARAQ for 28 h.

Simulation methods

To theoretically explore the relationship between the phase separation phenomena of WDR5 and CPC and their compartmentalization on chromosomes, we employed three-component Cahn–Hilliard equations. The dynamic evolution of the system was examined through numerical simulations. The phase separation behavior of WDR5 and CPC was modeled using the Flory–Huggins free energy model to derive the interaction free energy. Key parameters for the simulations included interaction coefficients, which were determined through qualitative comparisons with experimental data.

In the simulation of WDR5 and CPC molecular distribution on chromosomes, we introduced an external potential field, in addition to the interaction coefficients, to mimic the chromosomal structure and reflect the specific recruitment sites of WDR5 and CPC on the chromosome. Given that diffusion coefficients and molecular volumes for WDR5 and CPC had negligible effects on the qualitative behavior of the system, we approximated these values to be equal.

Details of the phase-field simulation

Equations for the phase separation droplet mixing system of WDR5 and CPC: with ϕ_W ϕ_C ϕ_S represent volume fraction of WDR5, CPC, and solvent, respectively.

$$\frac{\partial \phi_W}{\partial t} = \nabla \cdot \left[\lambda_W \nabla \left(\frac{\delta F_0}{\delta \phi_W} \right) \right]$$

$$\frac{\partial \phi_C}{\partial t} = \nabla \cdot \left[\lambda_C \nabla \left(\frac{\delta F_0}{\delta \phi_C} \right) \right]$$

$$\phi_W + \phi_C + \phi_S = 1$$

The expression for free energy F_0 writes:

$$\int dx \left[\begin{array}{c} \frac{\varepsilon^2}{2} \left(|\nabla \phi_W|^2 + |\nabla \phi_C|^2 \right) + \\ A \cdot \left(\phi_W \ln \phi_W + \phi_C \ln \phi_C + \phi_S \ln \phi_S + \chi_{WC} \phi_W \phi_C + \chi_{WS} \phi_W \phi_S + \chi_{CS} \phi_C \phi_S \right) \end{array} \right]$$

For parameters used in simulation, we set $\varepsilon = 10^{-2}$, $A = 0.2$, $\lambda_W = \lambda_C = 0.1$. Flory–Huggins interaction parameters χ are shown in the captions of the corresponding simulation diagram. Meanings of main parameters are as follows:

ε (gradient energy coefficient): Set to 10^{-2}, controlling the strength of the interfacial energy (surface tension). This order of magnitude is widely used in phase-field simulations, sufficient to drive

the system toward forming smooth interfaces while avoiding excessive numerical stiffness.

A (mixing free energy scale): Set to 0.2, adjusting the relative contribution of mixing entropy and mixing enthalpy terms. This value is referenced from simulation studies of classical Flory–Huggins multicomponent systems, allowing significant phase separation behavior within a reasonable concentration range.

λ (diffusion coefficient): Set as $\lambda_W = \lambda_C = 0.1$. We set the diffusion coefficients of the two components equal to simplify the model, focusing on the dominant role of thermodynamic interactions (controlled by the χ parameters) rather than kinetic differences. Minor variations in this parameter do not alter the qualitative conclusions reported in this work (such as phase structure and spatial separation patterns).

The selection of these fixed parameters aims to establish a robust simulation framework, enabling us to systematically investigate the effects of the key control parameters (namely, the χ interaction parameters).

Key interaction parameters (χ_{ws}, χ_{cs}, χ_{wc}): These parameters are the core variables studied in this work. Their specific values are based on experimental observations and the theory of multicomponent phase separation. For instance, $\chi_{ws} > \chi_{cs}$ reflects the stronger intrinsic phase separation tendency of WDR5 compared to ISB, while $\chi_{wc} > 0$ describes the repulsive interaction between the two.

For the simulation of WDR5 and CPC molecular distribution on chromosomes, the following external field was added:

$$F = F_0 + \int dx(\phi_W U_W + \phi_C U_C)$$

To model the recruitment behavior from chromosomes, we set $U_W = -0.5$ on the chromosome arm region, $U_C = -0.5$ on the centromere region, and $U_W = 0$, $U_C = 0$ everywhere else.

To simulate these equations, we discretized the spatial domain using two-dimensional grids. For time discretization, to enhance numerical stability, we adopted the semi-implicit scheme from a previous study[55]:

$$\frac{\phi_i^{n+1} - \phi_i^n}{\Delta t} = \nabla \cdot \left[\lambda_i \nabla \left(\frac{\partial F}{\partial \phi_i}\right)^n\right] + A\lambda_i \varepsilon^2 \nabla^4 \phi_i^n - A\lambda_i \varepsilon^2 \nabla^4 \phi_i^{n+1}$$

Here, the non-linear ∇^4 term serves as an artificial stabilization term. To mitigate numerical instabilities associated with high-order finite differences, we utilized Fourier transforms to solve the equations by converting between physical and spectral spaces. The numerical simulations were implemented using Python codes. Core computations, including the discretization of the governing equations and the evolution of the phase fields, were performed using the NumPy and SciPy libraries. All results were processed and visualized using Matplotlib.

Quantification and statistical analysis

For centromere-specific quantification of Aurora B, H3T3ph, and H3K4me3 levels, images were thresholded to define regions of interest ROIs based on anti-centromere antibody (ACA) signals. Fluorescence intensities of target proteins within ACA-demarcated centromeric regions were measured and normalized to ACA intensity to calculate the Aurora B/ACA, H3T3ph/ACA, and H3K4me3/ACA ratios.

For chromosome arm-specific quantification, chromosomal regions were first segmented using DNA staining, and ACA-defined centromeric areas were subtracted. Fluorescence intensities of Aurora B, H3T3ph, and H3K4me3 within the resulting arm ROIs were measured and normalized to ACA intensity.

Absolute fluorescence intensities at centromeres or chromosome arms were determined using Aurora B signals to define centromeric ROIs, with arm regions derived by subtracting centromeric areas from total chromosomal masks.

All statistical analyses were performed using GraphPad Prism v10.4.0. For comparisons between two independent groups, two-sided unpaired Student's t tests were used unless otherwise stated. For paired comparisons within the same cells, two-sided paired Student's t tests were used where appropriate. For comparisons among more than two groups, one-way ANOVA followed by Tukey's multiple-comparison test was used. Data are presented as mean ± SEM, with significance thresholds defined as $^{*}P < 0.05$, $^{**}P < 0.01$, $^{***}P < 0.001$, and $^{****}P < 0.0001$.

Reporting summary

Further information on research design is available in the Nature Portfolio Reporting Summary linked to this article.

Data availability

The Source Data file includes the numerical data underlying the quantifications presented in the main figures and Supplementary Figs., as well as uncropped and unprocessed scans of blots and gels. Source data are provided with this paper.

Code availability

The codes generated in this study are available on GitHub [https://github.com/jxyustc/NCL_CHSolver].

References

1. Bickmore, W. A. & van Steensel, B. Genome architecture: domain organization of interphase chromosomes. *Cell* **152**, 1270–1284 (2013).
2. Misteli, T. The self-organizing genome: principles of genome architecture and function. *Cell* **183**, 28–45 (2020).
3. Li, G. et al. Extensive promoter-centered chromatin interactions provide a topological basis for transcription regulation. *Cell* **148**, 84–98 (2012).
4. Dixon, J. R. et al. Chromatin architecture reorganization during stem cell differentiation. *Nature* **518**, 331–336 (2015).
5. Larson, A. G. et al. Liquid droplet formation by HP1α suggests a role for phase separation in heterochromatin. *Nature* **547**, 236–240 (2017).
6. Strom, A. R. et al. Phase separation drives heterochromatin domain formation. *Nature* **547**, 241–245 (2017).
7. Arnould, C. et al. Chromatin compartmentalization regulates the response to DNA damage. *Nature* **623**, 183–192 (2023).
8. Walczak, C. E., Cai, S. & Khodjakov, A. Mechanisms of chromosome behaviour during mitosis. *Nat. Rev. Mol. Cell Biol.* **11**, 91–102 (2010).
9. Jallepalli, P. V. & Lengauer, C. Chromosome segregation and cancer: cutting through the mystery. *Nat. Rev. Cancer* **1**, 109–117 (2001).
10. Jenuwein, T. & Allis, C. D. Translating the histone code. *Science* **293**, 1074–1080 (2001).
11. Kouzarides, T. Chromatin modifications and their function. *Cell* **128**, 693–705 (2007).
12. Stillman, B. Histone modifications: insights into their influence on gene expression. *Cell* **175**, 6–9 (2018).
13. Tian, Y. et al. Histone H1 deamidation facilitates chromatin relaxation for DNA repair. *Nature* **641**, 779–787 (2025).
14. Hirota, T., Lipp, J. J., Toh, B. H. & Peters, J. M. Histone H3 serine 10 phosphorylation by Aurora B causes HP1 dissociation from heterochromatin. *Nature* **438**, 1176–1180 (2005).
15. Ruchaud, S., Carmena, M. & Earnshaw, W. C. Chromosomal passengers: conducting cell division. *Nat. Rev. Mol. Cell Biol.* **8**, 798–812 (2007).
16. Carmena, M., Wheelock, M., Funabiki, H. & Earnshaw, W. C. The chromosomal passenger complex (CPC): from easy rider to the godfather of mitosis. *Nat. Rev. Mol. Cell Biol.* **13**, 789–803 (2012).

17. Liu, D., Vader, G., Vromans, M. J., Lampson, M. A. & Lens, S. M. Sensing chromosome bi-orientation by spatial separation of Aurora B kinase from kinetochore substrates. *Science* **323**, 1350–1353 (2009).
18. Lampson, M. A. & Cheeseman, I. M. Sensing centromere tension: Aurora B and the regulation of kinetochore function. *Trends Cell Biol.* **21**, 133–140 (2011).
19. Kelly, A. E. et al. Survivin reads phosphorylated histone H3 threonine 3 to activate the mitotic kinase Aurora B. *Science* **330**, 235–239 (2010).
20. Wang, F. et al. Histone H3 Thr-3 phosphorylation by Haspin positions Aurora B at centromeres in mitosis. *Science* **330**, 231–235 (2010).
21. Yamagishi, Y., Honda, T., Tanno, Y. & Watanabe, Y. Two histone marks establish the inner centromere and chromosome bi-orientation. *Science* **330**, 239–243 (2010).
22. Dai, J., Sullivan, B. A. & Higgins, J. M. Regulation of mitotic chromosome cohesion by Haspin and Aurora B. *Dev. Cell* **11**, 741–750 (2006).
23. Hyman, A. A., Weber, C. A. & Jülicher, F. Liquid-liquid phase separation in biology. *Annu. Rev. Cell. Dev. Biol.* **30**, 39–58 (2014).
24. Banani, S. F., Lee, H. O., Hyman, A. A. & Rosen, M. K. Biomolecular condensates: organizers of cellular biochemistry. *Nat. Rev. Mol. Cell Biol.* **18**, 285–298 (2017).
25. Boeynaems, S. et al. Protein phase separation: a new phase in cell biology. *Trends Cell Biol.* **28**, 420–435 (2018).
26. Song, X. et al. Phase separation of EB1 guides microtubule plus-end dynamics. *Nat. Cell Biol.* **25**, 79–91 (2022).
27. Ding, M. et al. A biophysical basis for the spreading behavior and limited diffusion of Xist. *Cell* **188**, e25 (2025).
28. Trivedi, P. et al. The inner centromere is a biomolecular condensate scaffolded by the chromosomal passenger complex. *Nat. Cell Biol.* **21**, 1127–1137 (2019).
29. Trivedi, P. & Stukenberg, P. T. A condensed view of the chromosome passenger complex. *Trends Cell Biol.* **30**, 676–687 (2020).
30. Sha, L. et al. Non-canonical MLL1 activity regulates centromeric phase separation and genome stability. *Nat. Cell Biol.* **25**, 1637–1649 (2023).
31. Hedtfeld, M., Dammers, A., Koerner, C. & Musacchio, A. A validation strategy to assess the role of phase separation as a determinant of macromolecular localization. *Mol. Cell* **84**, 1783–1801.e7 (2024).
32. Wysocka, J. et al. WDR5 associates with histone H3 methylated at K4 and is essential for H3 K4 methylation and vertebrate development. *Cell* **121**, 859–872 (2005).
33. Dou, Y. et al. Regulation of MLL1 H3K4 methyltransferase activity by its core components. *Nat. Struct. Mol. Biol.* **13**, 713–719 (2006).
34. Eswaran, J. et al. Structure and functional characterization of the atypical human kinase haspin. *Proc. Natl. Acad. Sci. USA* **106**, 20198–20203 (2009).
35. Varier, R. A. et al. A phospho/methyl switch at histone H3 regulates TFIID association with mitotic chromosomes. *EMBO J.* **29**, 3967–3978 (2010).
36. Oh, E. et al. Gene expression and cell identity controlled by anaphase-promoting complex. *Nature* **579**, 136–140 (2020).
37. Alberti, S., Gladfelter, A. & Mittag, T. Considerations and challenges in studying liquid-liquid phase separation and biomolecular condensates. *Cell* **176**, 419–434 (2019).
38. Shin, Y. et al. Spatiotemporal control of intracellular phase transitions using light-activated optoDroplets. *Cell* **168**, e14 (2017).
39. Zeitlin, S. G., Shelby, R. D. & Sullivan, K. F. CENP-A is phosphorylated by Aurora B kinase and plays an unexpected role in completion of cytokinesis. *J. Cell Biol.* **155**, 1147–1157 (2001).
40. Fischer, P. Polymer physics—applications to molecular association and thermoreversible gelation (F. Tanaka). *Appl. Rheol.* **22**, 235 (2012).
41. Yu, H. et al. HSP70 chaperones RNA-free TDP-43 into anisotropic intranuclear liquid spherical shells. *Science* **371**, eabb4309 (2021).
42. Feric, M. et al. Coexisting liquid phases underlie nucleolar subcompartments. *Cell* **165**, 1686–1697 (2016).
43. Dignon, G. L., Best, R. B. & Mittal, J. Biomolecular phase separation: from molecular driving forces to macroscopic properties. *Annu. Rev. Phys. Chem.* **71**, 53–75 (2020).
44. Phillips, M. & Ghosh, K. Rules of selective condensation in cells. *Nat. Chem.* **16**, 1042–1044 (2024).
45. Couture, J.-F., Collazo, E. & Trievel, R. C. Molecular recognition of histone H3 by the WD40 protein WDR5. *Nat. Struct. Mol. Biol.* **13**, 698–703 (2006).
46. Migliori, V. et al. Symmetric dimethylation of H3R2 is a newly identified histone mark that supports euchromatin maintenance. *Nat. Struct. Mol. Biol.* **19**, 136–144 (2012).
47. Zhao, J. et al. Structural insights into the recognition of histone H3Q5 serotonylation by WDR5. *Sci. Adv.* **7**, eabf4291 (2021).
48. Krüger, S., Weber, C. A., Sommer, J.-U. & Jülicher, F. Discontinuous switching of position of two coexisting phases. *N. J. Phys.* **20**, 075009 (2018).
49. Ali, A., Veeranki, S. N. & Tyagi, S. A SET-domain-independent role of WRAD complex in cell-cycle regulatory function of mixed lineage leukemia. *Nucleic Acids Res.* **42**, 7611–7624 (2014).
50. Guarnaccia, A. D. & Tansey, W. P. Moonlighting with WDR5: a cellular multitasker. *J. Clin. Med.* **7**, 21 (2018).
51. Neilsen, B. K. et al. WDR5 supports colon cancer cells by promoting methylation of H3K4 and suppressing DNA damage. *BMC Cancer* **18**, 673 (2018).
52. Lampson, M. A., Renduchitala, K., Khodjakov, A. & Kapoor, T. M. Correcting improper chromosome-spindle attachments during cell division. *Nat. Cell Biol.* **6**, 232–237 (2004).
53. Chen, F. et al. Predicting assembly mode of membraneless organelles by a FRET-based crowding sensor. *Signal Transduct. Target. Ther.* **8**, 227 (2023).
54. Alberti, S. et al. A user's guide for phase separation assays with purified proteins. *J. Mol. Biol.* **430**, 4806–4820 (2018).
55. Mao, S., Chakraverti-Wuerthwein, M. S., Gaudio, H. & Košmrlj, A. Designing the morphology of separated phases in multicomponent liquid mixtures. *Phys. Rev. Lett.* **125**, 218003 (2020).

Acknowledgements

We are grateful to all current and former members of the D.L. laboratory for providing materials and helpful discussions. The simulations were performed on the robotic AI-Scientist platform of the Chinese Academy of Sciences.

Author contributions

Y.W., Xianyun Jiang, X.L., X.Y., Z.H., and D.L. conceptualized the study. Y.W., Xianyun Jiang, X.L., X.S., F.C., A.T., X.Y., Z.H., and D.L. developed the methodology. Y.W., Xianyun Jiang, and Y.L. performed formal analysis. Y.W., Xianyun Jiang, X.W., Y.L., and X.G. carried out the investigation. A.T., S.S., X.Y., Z.H., and D.L. provided resources. Y.W., Xianyun Jiang, X.L., Xin Jiang, and D.L. curated the data. Y.W., Xianyun Jiang, and D.L. wrote the original draft. S.S., X.Y., Z.H., and D.L. reviewed and edited the manuscript. Y.W., Xianyun Jiang, and Xin Jiang prepared the visualizations. S.S., X.Y., Z.H., and D.L. supervised the work. D.L. administered the project. X.Y., Z.H., and D.L. acquired funding.

Funding

This work was supported by the National Natural Science Foundation of China, grant numbers 32090041 to D.L., 32521003 to X.L., 22533005 to Z.H., and 32090040 to Z.H. and X.Y.; the National Key Research and Development Program of China, Ministry of Science and Technology of the People's Republic of China, grant numbers 2016YFA0101200 to D.L. and 2022YFA1303100 to Z.H. and X.Y.; the Fundamental and

Interdisciplinary Disciplines Breakthrough Plan of the Ministry of Education of China, grant number JYB2025XDXM505 to Z.H.; and the Strategic Priority Research Program of the Chinese Academy of Sciences, grant number XDB0450402 to Z.H.

Competing interests
The authors declare no competing interests.

Additional information
Supplementary information The online version contains supplementary material available at https://doi.org/10.1038/s41467-026-74446-6.

Correspondence and requests for materials should be addressed to Sibei Sheng, Xuebiao Yao, Zhonghuai Hou or Dan Liu.

Peer review information *Nature Communications* thanks Daniel Booth, who co-reviewed with Charles CresswellP. Todd Stukenberg and the other, anonymous, reviewer(s) for their contribution to the peer review of this work. A peer review file is available.